THE EUROPEAN
PHYSICAL JOURNAL PLUS

Regular Article

Assessing the 3D resolution of refocused correlation plenoptic images using a general-purpose image quality estimator

Gianlorenzo Massaro[1,2,a]

[1] Dipartimento Interateneo di Fisica, Universitá degli Studi di Bari, Via Giovanni Amendola, 173, 70125 Bari, Italy
[2] Istituto Nazionale di Fisica Nucleare, Sezione di Bari, Via Giovanni Amendola, 173, 70125 Bari, Italy

© The Author(s) 2024

Abstract Correlation plenoptic imaging (CPI) is emerging as a promising approach to light-field imaging (LFI), a technique enabling simultaneous measurement of light intensity distribution and propagation direction from a scene. LFI allows single-shot 3D sampling, offering fast 3D reconstruction for a wide range of applications. However, the array of micro-lenses typically used in LFI to obtain 3D information limits image resolution, which rapidly declines with enhanced volumetric reconstruction capabilities. CPI addresses this limitation by decoupling the measurement of the light field on two photodetectors with spatial resolution, eliminating the need for micro-lenses. 3D information is encoded in a four-dimensional correlation function, which is decoded in post-processing to reconstruct images without the resolution loss seen in conventional LFI. This paper evaluates the tomographic performance of CPI, demonstrating that the refocusing reconstruction method provides axial sectioning capabilities comparable to conventional imaging systems. A general-purpose analytical approach based on image fidelity is proposed to quantitatively study axial and lateral resolution. The analysis fully characterizes the volumetric resolution of any CPI architecture, offering a comprehensive evaluation of its imaging performance.

1 Introduction

Correlations of light have long been a subject of study due to their potential to enhance the capabilities of traditional measurement techniques [1–8]. In both classical and quantum contexts, the exploration of correlations has led to significant advancements, particularly in imaging technologies [9–24]. In the quantum domain, the unique properties of entanglement and correlation have been harnessed to surpass the sensitivity limits of conventional imaging methods [25]. This has enabled breakthroughs, such as sub-shot-noise microscopy [26, 27], providing unprecedented precision in imaging amplitude and phase samples [28]. Interestingly, correlation properties similar to those obtained with quantum states of light can also be observed in classical systems. This convergence of quantum and classical approaches has revealed that many protocols initially designed for quantum applications can be effectively adapted to classical contexts [9, 29–32]. Consequently, the study of correlations continues to bridge the gap between quantum and classical imaging, offering versatile solutions that transcend the traditional boundaries of these domains. Correlation plenoptic imaging (CPI) [33–39] is emerging as a promising correlation-based approach to light-field imaging (LFI). LFI is a technique that allows for the concurrent measurement of both light intensity distribution and propagation direction of light rays from a three-dimensional scene of interest [40]. The extensive amount of information collected by a light-field device enables single-shot 3D sampling, a task that would require multiple acquisitions across various planes with a standard camera [41, 42]. This scanning-free characteristic makes light-field imaging one of the fastest methods for 3D reconstruction, with applications spanning diverse fields such as photography [43–45], microscopy [46] and real-time imaging of neuronal activity [47]. In its typical implementation, light-field imaging employs an array of micro-lenses positioned between the sensor and the imaging device (e.g., the camera lens). These lenslets generate a series of "sub-images" corresponding to different propagation directions. However, the presence of the array significantly limits image resolution, preventing it from reaching the diffraction limit and causing a rapid decline in resolution as 3D reconstruction capabilities improve [48, 49]. CPI addresses the main limitation of conventional LFI by decoupling the measurement of light-field information on two photodetectors endowed with spatial resolution [33], in a lenslets-free optical design. In fact, three-dimensional information about the sample is encoded in the four-dimensional correlation function, obtained by correlating the instantaneous light intensity impinging on the sensors and performing statistical averaging. The correlation function can then be decoded, entirely in post processing, to reconstruct high-resolution images of the object without the loss of resolution typical of conventional LFI.

[a] e-mail: gianlorenzo.massaro@uniba.it (corresponding author)

Springer

In this paper, we shall evaluate the tomographic performance of CPI, showing that the reconstruction approach called *refocusing* [50] endows CPI with the same axial sectioning capabilities of a conventional imaging system, in which fine axial sectioning is obtained by increasing the size of the optical elements. After a quantitative study of the axial depth of the reconstructed images, an analytical approach based on the *image fidelity* [51] shall be proposed. Through the fidelity analysis, the axial and lateral resolution of CPI be studied quantitatively, in a more general and formally sound approach, compared to the past, and can be applied to evaluate the imaging performance of any CPI architecture. Such mathematical tool will thus be used to fully characterize, analytically and through numerical analysis, the 3D resolution of CPI.

2 Image reconstruction in CPI

In CPI, light-field information about the sample is collected by measuring intensity (or photon number) correlations on two detectors with spatial resolution. The measured correlation function reads

$$\Gamma(\boldsymbol{r}_a, \boldsymbol{r}_b) = \langle I_A(\boldsymbol{r}_a) I_B(\boldsymbol{r}_b) \rangle - \kappa \langle I_A(\boldsymbol{r}_a) \rangle \langle I_B(\boldsymbol{r}_b) \rangle, \tag{1}$$

where $I_{A,B}$ is the instantaneous light intensity on the detectors [52], and $\boldsymbol{r}_{a,b} = (x_{a,b}, y_{a,b})$ is the two-dimensional coordinate on the two detectors surface; the symbol $\langle I \rangle$ denotes the ensemble average of the statistical quantity I. The constant $\kappa = 0, 1$ can vary according to the illumination source of choice for performing CPI: in fact, when illuminating with entangled photons, light-field information is collected by evaluating photon number correlations ($\kappa = 0$) [53–55], whereas, for thermal and pseudo-thermal light, intensity *fluctuations* should be measured ($\kappa = 1$) [34, 36, 55, 56]. Without loss of generality, we shall henceforth assume that CPI is performed with pseudo-thermal illumination ($\kappa = 1$), and shall also neglect the four-dimensional dependence of the correlation function, to limit ourselves only to the x-component of the detectors coordinate.

Despite CPI can be implemented in many possible variations, from a fundamental point of view, the mathematical description of the correlation function can be explained by means of a second-order response function Φ': in fact, regardless of the particular architecture

$$\Gamma(x_a, x_b) = \left| \int A(x_s) \int \left[A^*(x_s') \right]^m \Phi'(x_s, x_s', x_a, x_b) \, dx_s' \, dx_s \right|^2. \tag{2}$$

Eq. (2) establishes the relationship between the electric field at the detectors coordinates $x_{a,b}$, and the field at the sample coordinates x_s[1]; the function $A(x_s)$ represents the complex electric field transmittance of a flat sample, and the coefficient m can either be 0, if only one of the two detectors collects light from the object, or 1 if light from the sample illuminates both sensors [52]. In the most general case, the optical response of CPI is thus strongly nonlinear with respect to the input function A, both because A is involved twice due to a second-order response function, and because of the square module taken after the integrals. In many cases of interest, however, such degree of complexity is not required to fully predict the optical performance of CPI. For instance, when only one detector collects light from the sample ($m = 0$), the system is described by a *complex* first-order response function (or complex point spread function, PSF) $\Phi(x_s, x_a, x_b) = \int \Phi(x_s, x_s', x_a, x_b) \, dx_s'$. On the other hand, for CPI schemes characterized by $m = 1$, a second-order response function results from effects of partial coherence on the sample surface, namely, from non-negligible coherence area on the object. Such effects, however, can either be neglected, as is the case when the sample itself is the source of thermal light, or should be avoided through careful optical design, e.g. when working with transmissive samples. By neglecting partial coherence on the source, the response function of the system becomes $\Phi'(x_s, x_s', x_a, x_b) \sim \delta(x_s - x_s') \Phi(x_s, x_a, x_b)$, so that Eq. (2) can be written as

$$\Gamma(x_a, x_b) = \left| \int A(x_s) \left[A^*(x_s) \right]^m \Phi(x_s, x_a, x_b) \, dx_s \right|^2. \tag{3}$$

From Eq. (3), one immediately recognizes that the only difference between architectures characterized by $m = 0$ and $m = 1$ is that the former are sensitive to the phase content of the complex function A, whereas the latter are only sensitive to the intensity profile of the object $|A|^2$. This distinction does not have any influence on the optical performance of the technique, so we shall limit our discussion to phase-insensitive architectures, characterized by negligible coherence area on the sample surface.

To some extent, some information about the sample can be inferred already from the correlation function itself [52]; however, in order to gain axial localization of the sample features and dramatically improve the signal to noise ratio (SNR) [57, 58], the Γ function must be *refocused* to obtain a sharp image of the sample. As outlined in Refs. [50, 52, 54], the reasoning behind the refocusing procedure is based entirely on geometrical optics arguments, i.e., on ray-tracing. Through refocusing, a specific object coordinate (x_s, z) is reconstructed by summing together all the correlated optical paths leading to the two detectors, crossing the object plane at axial coordinate z and transverse coordinate x_s. In fact, in a geometrical optics approximation [52], the correlation function measured when the object $A(x_s)$ is placed at an axial coordinate z is approximately given by

$$\Gamma(x_a, x_b) \sim |A(\alpha(z) \, x_a + \beta(z) \, x_b)|^{2(m+1)}, \tag{4}$$

---

[1] Eq. (4) in Ref. [52].

Fig. 1 Schematics of a single-lens CPI scheme
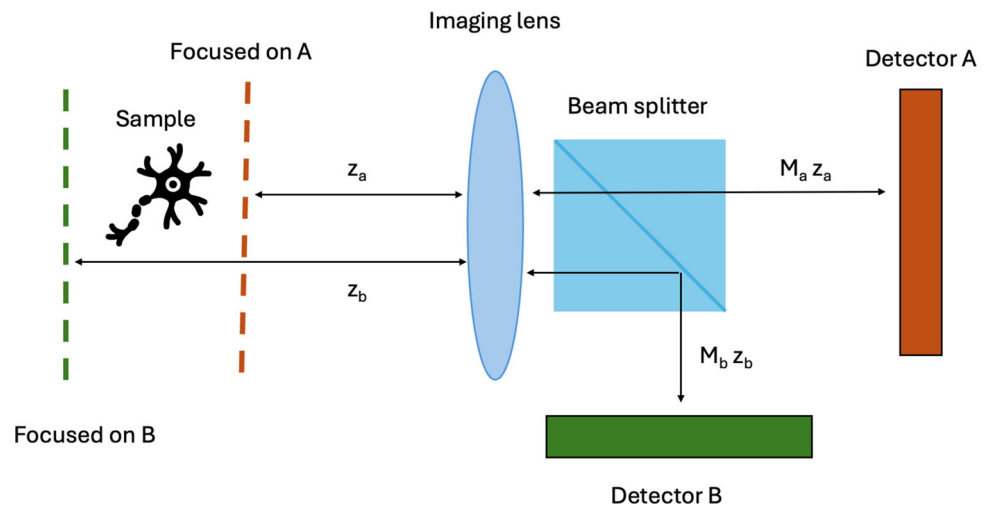
where the coefficients $\alpha(z)$ and $\beta(z)$ depend both on z and on the optical design of the experiment. Hence, the geometrical locus of points corresponding to the same object coordinate x_s in the (x_a, x_b) space is a straight line of equation

$$\gamma(x_s, z) : \alpha(z)\, x_a + \beta(z)\, x_b = x_s. \tag{5}$$

In order to extract all the possible information about x_s from the correlation function, one must integrate along γ, so that the reconstructed image is obtained by performing a line integral

$$\Sigma_z(x_s) = \int_{\gamma(x_s,z)} \Gamma \, d\ell. \tag{6}$$

As specified in Eq. (5), the axial plane that is reconstructed is entirely determined by the coefficients $\alpha(z)$ and $\beta(z)$.

3 Axial sectioning

Because of the geometry of the integration path reconstructing a sample coordinate x_s, Eq. (6) can be recognized as a Radon transform of the correlation function at an angle $\theta(z) = -\arctan[\alpha(z)/\beta(z)]$ so that, in the formalism conventionally used for techniques based on tomographic reconstruction through Radon transformation [59],

$$\Sigma_z(x_s) = R\Gamma(\theta, x_s) = \int_{-\infty}^{+\infty} \Gamma\big(x'\,\sin\theta + x_s\,\cos\theta, \ -x'\,\cos\theta + x_s\,\sin\theta\big) dx'. \tag{7}$$

Such an analogy allows us to promptly infer that, as with any tomographic technique based on back-projection reconstruction, the "depth" of the reconstructed images can be expected to depend on the number of directions in the Fourier domain available for the reconstruction [44, 60], or, equivalently, on the length of the integration path $\gamma(x_s, z)$ in Eq. (6). In other words, the axial sectioning of CPI can be associated to the extension of the support of the correlation function which, as demonstrated both theoretically [50, 52] and experimentally [35], depends on the size of the optics, namely, on the numerical aperture (NA).

For definiteness, all the results presented in the paper are obtained on a CPI architecture based on a single-lens design [55], schematically represented in Fig. 1. In this architecture, the two detectors A and B are optically conjugated, by means of an imaging lens, to two planes in the region of space occupied by the sample. We shall indicate with z_A (z_B) the optical distance between the object plane imaged on detector A (B) and the lens, so that the plane is imaged with magnification M_a (M_b), as defined by the optical distances involved and the focal length f of the lens. After the lens, light coming from the sample is separated into to two optical paths leading toward the detectors by means of a beam-splitter.

The tomographic capabilities of CPI are better understood through direct comparison with a conventional imaging system, based on a single-lens design and on intensity measurement (for instance, if only measuring the intensity I_A impinging on detector A). In such systems, the axial scanning of the 3D space surrounding the sample is performed mechanically, by varying the relative distance between the detector and lens, so that a stack of different planes at focus is available after the measurement. The quality of the axial scanning depends on how effectively the imaging system suppresses, at any given focusing position, spurious contributions from unfocused planes, namely, on the thickness of the depth of field (DOF). Suppression of background planes in conventional imaging is knowingly due to the circle of confusion (COC) [61], a mechanism that is entirely explained in terms of ray optics, which makes so that point-like objects in the background produce a circle-shape projection onto the plane on focus. Such effect is increasingly more relevant as the NA of the system increases, so that high-NA designs are not only beneficial because of the high resolution they
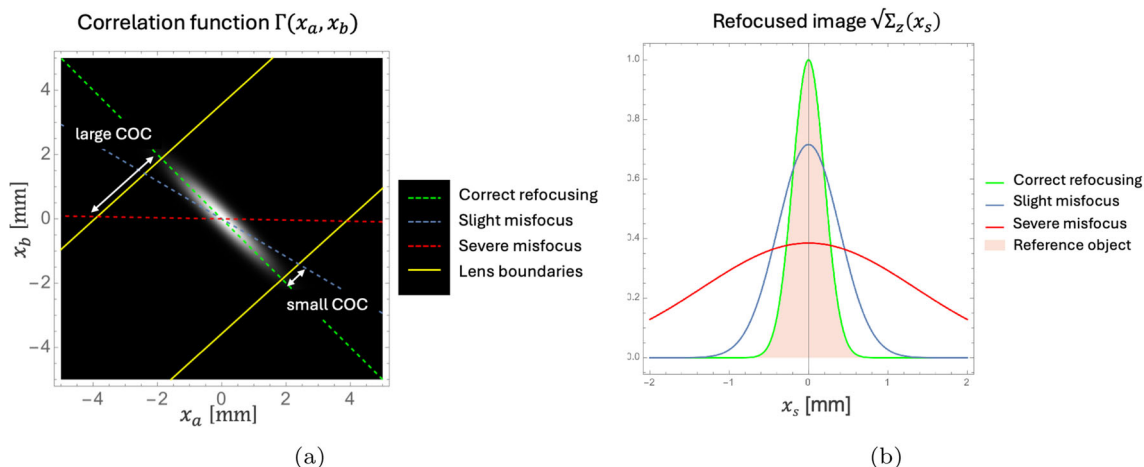
Fig. 2 *Panel* **a** Measured correlation function in the case of a Gaussian-slit object, placed on the optical axis at $z_s = (z_a + z_b)/2$; *Panel* **b** comparison between a proper refocusing $\sqrt{\Sigma_z}$ with $z = z_s$ and an incorrect refocusing at $z \neq z_s$

provide at focus, but also because of their shallow DOF [62]. We shall now demonstrate that CPI benefits from the same high-NA design, as far as axial sectioning is concerned.

Figure 2a reports an example of a measured correlation function $\Gamma(x_a, x_b)$, obtained by simulating the optical setup in Fig. 1. To obtain the correlation function, we set the focal length of the imaging lens to $f = 75$ mm; detectors A and B image their respective conjugate planes with magnifications $M_a = 1.1$ and $M_b = 0.9$, thus resulting in $z_a \simeq 143$ mm and $z_b \simeq 158$ mm. For ease of calculation, we have assumed the lens pupil has Gaussian apodization, with a width of $\sigma_l = 25$ mm. The plot is obtained by assuming that the imaged object is a Gaussian transmissive slit having intensity profile

$$|A(x_s)|^2 = \exp\left[-\frac{x_s^2}{2\sigma_s^2}\right], \tag{8}$$

with $\sigma_s = 200\,\mu$m. For the case shown in Fig. 2a, the object is placed on the optical axis at a distance $z_s = (z_a + z_b)/2$ from the lens, so that neither A nor B yield a focused image of the sample. For this CPI architecture, the object coordinate x_s of a sample placed at a generic axial distance z is reconstructed by integrating along the line

$$\gamma(x_s, z) : x_s = -\frac{z - z_b}{z_a - z_b}\frac{x_a}{M_a} + \frac{z - z_a}{z_a - z_b}\frac{x_b}{M_b}. \tag{9}$$

Therefore, an object placed mid-way between z_a and z_b is correctly reconstructed via a Radon transformation at an angle $\theta(z = z_s) = -\pi/4$, as is evident from the picture (the dashed green line is parallel to the object features). As is the case for standard imaging, however, one does not typically know *a priori* the correct axial position of the sample. Hence, a complete z-scan of the 3D space surrounding the sample is usually needed. This entails calculating Radon transformations at many different angles $\theta(z) \neq \theta(z_s)$ which can be expected to result in a less sharp image than perfect refocus $\theta(z_s)$, and also to a suppression of the intensity peak, as is the case for out-of-focus imaging in a conventional scenario. Rather intuitively, this effect must be the analogous of the COC, since the blurring of misfocused plane can easily be envisioned to depend on how extended the integration paths are (as defined by the NA), and on how misfocused the integration angle is with respect to the correct one. Such picture can be graphically verified from Fig. 2a, where we reported the lens boundaries (yellow lines, corresponding to the projection of the lens coordinates at $\pm 3/2\,\sigma_l$ onto the (x_a, x_b) plane), and two integration angles corresponding to $z = 152$ mm $\neq z_s$ (dashed blue line), and $z = z_b \neq z_s$ (dashed red line). In fact, the extent of blurring can clearly be expected to be directly proportional to both the difference of the lines slope, with respect to the green line, and to how large the NA of the lens is (distance between the yellow lines). This is verified in Fig. 2b, demonstrating that the best reconstruction (green line) happens when integrating at $\theta(z_z)$ and results in an image indistinguishable from the reference object (solid salmon area). For the other integration directions (solid blue and red lines), slight and severe blurring occur, respectively, so that the final reconstruction results in a blurred and fainter image.

3.1 Quantitative analysis of the axial sectioning

From a qualitative point of view, the results shown in Figs. 2a and b hint that the tomographic capabilities of the refocusing algorithm are related to the COC. This can also be proved quantitatively, by studying how faithfully CPI can reconstruct the image of an object placed at a given axial coordinate. In order to do so, we shall use a newly introduced tool for evaluating image quality, named the
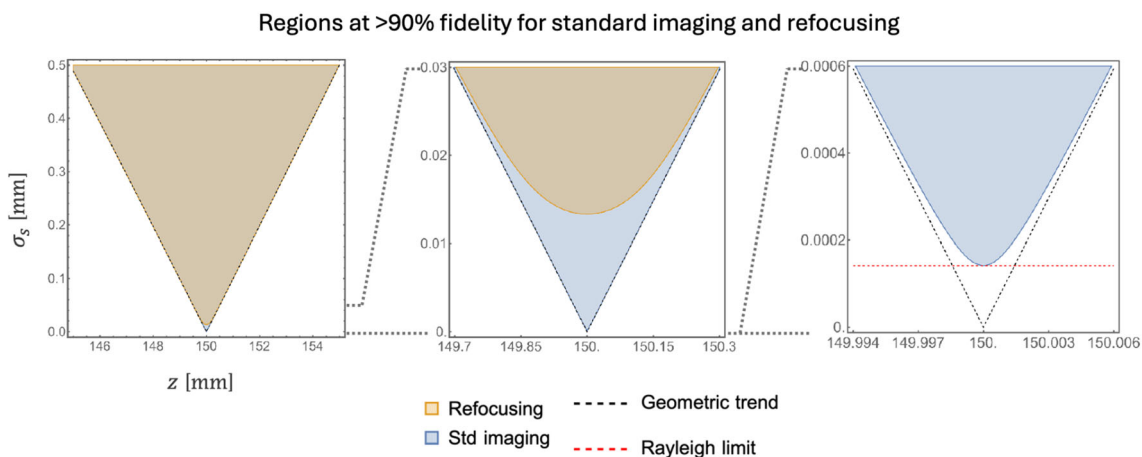
Fig. 3 Curves characterized by image fidelity larger than 90% in the (z, σ_s) space

image fidelity [51]. If an imaging system produces an image $I(x_s)$ of a sample with intensity transmittance $|A(x_s)|^2$, the fidelity $F_A[I]$ is defined as

$$F_A[I] = \int \sqrt{I(x)|A(x)|^2}\,dx; \tag{10}$$

where the quantities involved must be properly normalized ($\int I(x_s)\,dx_s = 1$ and $\int |A(x_s)|^2\,dx_s = 1$). $F_A[I]$ saturates to unity for perfectly accurate imaging systems, namely $I(x) = |A(x)|^2$, and approaches 0 for very unfaithful imaging. The analysis in terms of fidelity enables us to obtain *fidelity curves* that fully characterize the optical performance of the technique in terms of the experimental parameters, and replace the concept of *resolution* in imaging modalities where such a concept cannot be as clearly defined as in standard imaging [51].

To fully characterize the analogies with the COC of a misfocused imaging system, we shall compare the fidelity of a CPI refocusing z-scan directly with the fidelity of the mechanical z-scan of a standard imaging system, having the same optical design as a single arm of our CPI scheme. If an object of size σ_s is fixed at a distance z_s from the lens, an axial scan is obtained by moving the detector-to-lens distance so as to change the z in focus; in this context, the resulting image depends on both parameters z_s and z. Overall, the image resulting from an intensity measurement depends on three parameters, and we shall indicated it as $I_{\text{std}}(x; z, z_s, \sigma_s)$, where x is the image coordinate. If an object is placed at z_s, also the image reconstructed through CPI refocus $\Sigma_z(x; x_s, \sigma_s)$ depends on the same three parameters, with the difference that z-scanning is obtained through Radon transformation and not by mechanical movement of the detector. For our analysis, both z_a and z_b will be considered to be fixed. The fidelity of a standard and refocused image are evaluated, respectively, as

$$F_A[I_{\text{std}}](z, z_s, \sigma_s) = \int \sqrt{I_{\text{std}}(-M(z)\,x_s, z, z_s, \sigma_s)\,|A(x_s, \sigma_s)|^2}\,dx_s \tag{11}$$

$$F_A[\Sigma_z](z, z_s, \sigma_s) = \int \sqrt{\sqrt{\Sigma_z(x_s; z_s, \sigma_s)}\,|A(x_s, \sigma_s)|^2}\,dx_s. \tag{12}$$

The two definitions are adapted so as to compare the results as fairly as possible. In fact, the optical magnification of the imaging system $M(z)$ has been introduced in Eq. (11) to scale the image to its original size on the object side of the lens; such operation is not necessary in CPI, since it is included in the refocusing procedure [50]. Since the z-scanning is obtained by changing the detector position, each plane in focus is imaged with a different magnification, originating the dependence of M on z. The additional square root on Σ_z has been introduced in Eq. (12) to compensate for the known fact that, even in perfect imaging conditions, CPI returns the *squared* intensity profile of the sample when both detectors see light from the object (see Eq. (2) when $m = 1$).

In Fig. 3, we report the results of the fidelity analysis for standard imaging and CPI refocusing. The analysis has been carried out by considering a Gaussian object of width σ_s, placed at a fixed distance $z_s = (z_a + z_b)/2 = 150$ mm from the lens, for both CPI and standard imaging. The experimental parameters z_a, z_b, f and σ_l have been fixed to the same values as in Fig. 2a. Since the object is at a fixed coordinate, the fidelity of Eqs. (11) and (12) reduces to a two-variable function of the object size σ_s and scanning coordinate z. The blue area, corresponding to refocusing, and orange area, corresponding to standard imaging, identify the region of the (z, σ_s) space in which a sample can be imaged, by the corresponding technique, with fidelity larger than 90%. Hence, at any given object size σ_s, the difference between the largest and smallest z at which an object is imaged with 90% fidelity can be regarded as the axial resolution, or DOF, of the technique. As we can see, for large object sizes and large displacements (leftmost panel), refocusing

Fig. 4 Fidelity analysis in the plane of sharpest reconstruction $\Sigma_{z=z_s}$
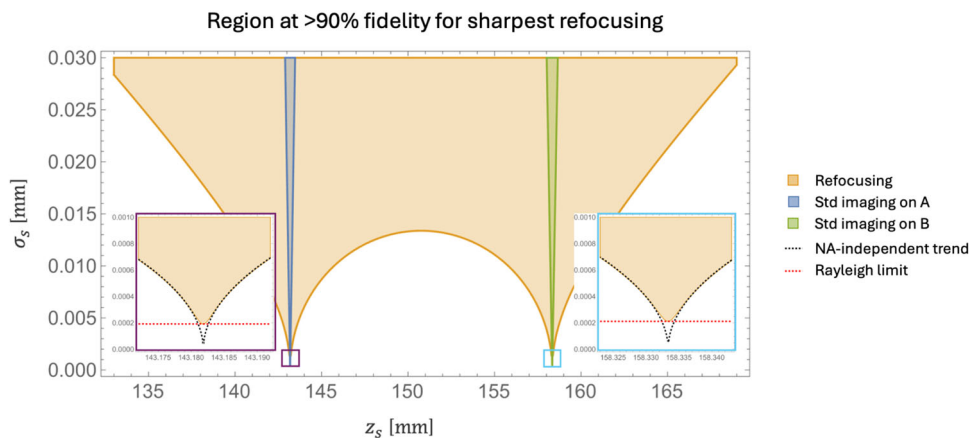
shows exactly the same performance as conventional imaging, which is knowingly limited by the COC. Considering the COC is a ray optics concept, it is worth investigating the behavior of $F_A[\Sigma_z]$ in the geometrical optics approximation for refocusing, namely

$$F_{\text{geom}}(z, z_s, \sigma_l) = \lim_{\lambda \to 0} F_A[\Sigma_z](z, z_s, \sigma_l). \tag{13}$$

The implicit equation $F_{\text{geom}}(z, z_s, \sigma_l) = c$, identifying the curve at fidelity c in the (z, z_s, σ_l) space, can be easily inverted to obtain the minimum size of the object that can faithfully be reconstructed, as a function z and z_s

$$\sigma_{\text{geom}}(z, z_s) \simeq |z - z_s| \frac{\sigma_l}{z_s} f(c), \tag{14}$$

where $f(c)$ is a function of the threshold value c, arbitrarily chosen to discriminate between faithful and unfaithful images. As predicted, the expression of σ_{geom} is exactly the same as the COC in conventional imaging, being directly proportional to both the *effective* numerical aperture σ_l/z_s, and to the relative displacement from the plane of sharpest reconstruction. As can be seen from Fig. 3, where Eq. (14) is reported as a dashed black line, when the object size is far from the lateral resolution limit of the techniques at the given z_s, the optical performance of both standard imaging and refocusing is determined by ray optics. In this condition, one obtains that the thickness of a reconstructed image at any given object size is

$$\text{DOF}_\Sigma(\sigma_S) \propto \frac{\sigma_s}{\text{NA}}, \tag{15}$$

as for a standard imaging system.

4 Lateral resolution of CPI

In the middle panel of Fig. 3, we see that when the object size approaches the resolution limit of CPI at the object position z_s, the optical performance of refocusing detaches from the geometrical trend, which would incorrectly prescribe a point-like resolution ($\sigma_{\text{geom}}(z = z_s, z_s) = 0$). A conventional z-scanning imaging system, however, still behaves according to geometrical optics at that scale, detaching from it only when the Rayleigh limit ($\propto \lambda/\text{NA}$) is reached (right panel). The fact that, at any given transverse plane z_s, the resolution of CPI refocusing is worse than a conventional imaging system is a known fact. For a CPI architecture such as the one we are considering, in fact, only two planes can be knowingly reconstructed at Rayleigh-limited resolution, namely, the planes at distance z_a and z_b, which are optically conjugated to the detectors [55].

As opposed to the previous section, we shall now analyze the image quality of a refocused image as the object is moved along the optical axis, by disregarding the axial depth of the reconstructions. This corresponds to studying the case in which, for any given object placement z_s one does not consider the whole z-scanning Σ_z, but only the sharpest reconstruction $\Sigma_{z=z_s}$. Through Eq. (12), we can thus evaluate the performance of CPI in the plane of best refocusing, namely $F_A[\Sigma_z](z = z_s, z_s, \sigma_s)$. For reference, we shall also report the image quality obtained by detectors A and B without the use of correlations, to show the performance improvement granted by the correlation measurement. The fidelity of the images collected on the detectors, separately, can be evaluated through Eq. (11), as $F_A[I_{\text{std}}](z = z_{a,b}, z_s, \sigma_s)$, at the two fixed experimental values z_a and z_b.

The fidelity analysis in the plane of sharpest reconstruction is reported in Fig. 4. As already well known, the DOF of CPI is much larger than the DOF of the two conventional single-lens systems measuring intensity on A and on B (blue and green areas, respectively). As in the previous case, we define the DOF as the difference between the largest and smallest z_s that allow for a faithful image reconstruction at a given object size. We should point out, however, that the meaning of DOF in this context is different from the previous section. In fact, the previous DOF was an estimation of the "depth" of the reconstruction, whereas now it is the axial range in which CPI can successfully reconstruct an object of given size σ_s. The difference can be understood by considering that

the previous analysis was carried out by considering a *fixed object* at coordinate z_s, while the analysis reported in Fig. 4 evaluates the best possible refocusing at any object coordinate. In other terms, if the analysis of Fig. 3 is useful for evaluating the DOF of a refocused image, Fig. 4 allows one to evaluate the DOF of the technique itself. The DOF of the reconstruction should then be regarded as the *axial resolution* of the technique, so that the ratio between the two determines the number of independent planes in the overall DOF of the technique that can be *isolated* through refocusing.

The *fidelity curves* of Fig. 4 must be intended as a replacement for the *visibility* or *resolution curves* of CPI, presented in previous literature [33–35, 54–56]. For reason that will be clarified shortly, however, the fidelity curves represent a much more general way of estimating the optical performance of CPI. The lower boundary to the orange areas of the figure represents the parametric curve $F_A[\Sigma_z](z = z_s, z_s, \sigma_s) = 0.9$, namely, the 90%-fidelity curve in the (z_s, σ_s) plane. Such curve thus establishes a correspondence between the axial coordinate z_s and the minimum object size $\sigma_{\min}(z_s)$ that can be reconstructed faithfully enough at that position. It is already known that the functional relationship $\sigma_{\min}(z_s)$ is for the most part independent of the numerical aperture of the setup, with the exception of the planes in focus ($z_s = z_a$ and $z_s = z_b$), which are available with Rayleigh-limited resolution. Such independence of the optical performance of CPI from NA sets the technique apart from conventional imaging for which, as we detailed in the previous section, the defocused optical performance is defined by the NA-proportional COC. One can thus check whether the performance of CPI can be predicted independently on NA even from an analytical point of view, by studying the fidelity of an ideal system

$$F_\infty(z_s, \sigma_s) = \lim_{\text{NA} \to \infty} F_A[\Sigma_z](z = z_s, z_s, \sigma_s). \tag{16}$$

Also in this case, the implicit equation of the c-fidelity curve $F_\infty(x_s, \sigma_l) = c$ can be inverted, so that the fidelity curve in the infinite-NA case reads

$$\sigma_\infty(z_s) \simeq \sqrt{\lambda \left| \frac{1}{z - z_a} - \frac{1}{z - z_b} \right|^{-1}} \, f'(c). \tag{17}$$

The infinite-NA fidelity curve is reported in the two insets in Fig. 4, showing the details of the CPI fidelity in very close proximity to the two axial planes in focus. The plot demonstrates that, apart from a very small region of space in which the resolution is defined by the NA-dependent Rayleigh limit[2] ($\propto \lambda/\text{NA}$), the optical performance of CPI reproduces with extreme accuracy the trend associated to the infinite-NA regime. The mechanism responsible for the loss of resolution of CPI outside of the natural DOF of the lens is thus completely independent of the optics size.

5 Conclusions

The surprising independence of the lateral resolution of CPI on the NA of the imaging system, with the exception of the plane (or planes) in focus, was already known in previous literature and even proven experimentally [35]. The origin of such property was, however, not clearly understood, mostly because of two aspects: firstly, the exact mathematical relationship between the form of the refocused image and the object is not known, and, secondly, because the image quality of CPI has been so far assessed by using conventional image quality estimators (e.g. "two-point" resolution, maxima-minima visibility, modulation transfer function (MTF) analysis). Such estimators are unfit to correctly evaluate the performance of CPI: from Eq. (3), it is rather evident that the technique, even without considering the added degree of complexity introduced by refocusing, is a *non-linear* imaging method, in the sense that the input signal $|A(x)|^2$ is not related to the output image through a simple *transfer function*, as is the case for conventional imaging systems. In standard imaging, in fact, the only mechanism[3] responsible for image quality degradation is blurring or, equivalently, the fact that the final image is obtained by convolution of the input with a *positive* PSF. Because of this property, all the merit figures conventionally used for image quality assessment can be reduced to the underlying linearity of the imaging formation process, and can thus be applied to a limited extent to predict the performance of nonlinear imaging [51]. In this work, we have decided to base our analysis of the optical performance of CPI on the image fidelity, which, being independent of the details of the image formation process, allows for a direct and *unbiased* comparison to other techniques. Through the fidelity analysis, we have demonstrated that the same results and NA-independence of the lateral resolution in the plane of best refocusing can be obtained in a mathematically consistent formalism, which has the advantage of not relying on assumptions on the imaging formation process. Compared to an assessment through image visibility, typically used in literature to evaluate the performance of CPI [54, 55], the fidelity has the advantage of being based on the *global* features of the image, and not on the very local nature of maxima and minima. Furthermore, compared to visibility, the fidelity is always an increasing function of the object size, when all the other parameters are fixed,

---

[2] From both Figs. 3 and 4, the Rayleigh limit prescribed by the fidelity analysis (red dashed line) is much smaller than $1.22\,\lambda/\text{NA}$, namely, the value of the Rayleigh limit that is obtained in a standard treatment. Such discrepancy with our case is due to fact that the fidelity analysis should not be interpreted as the size of a PSF, which is the origin of the conventional 1.22 coefficient. As outlined in detail in Ref. [51], the Rayleigh limit in the fidelity on focus is recognized by the typical dependence on the ratio λ/NA, whereas the proportionality constant results from an arbitrary choice for the fidelity threshold c.

[3] If aberrations are neglected.

$$\frac{\partial F_A[\Sigma_z]}{\partial \sigma_s}(z, z_s, \sigma_s) > 0,$$

and does not show any unphysical fluctuating behavior [54, 55, 63, 64]. Most importantly, the results that we presented in this work only for the case of the optical design of Fig. 1, have been obtained also by extending the study to other CPI architectures; in all cases, the fidelity analysis has confirmed the NA independence and square-root trend of the lateral resolution of CPI that was already known in literature. Through the fidelity analysis we have confirmed that the fidelity curves in the plane of best refocusing are always given by a square-root law, independently of the architecture

$$\sigma_\infty(z_s) \propto \sqrt{\lambda \, |d(z_s)|}; \tag{18}$$

the "equivalent distance" $d(z_s)$ is, however, a function of the CPI architecture at hand. For instance, for CPI architectures based on position-momentum correlations [56], $d(z_s) = z_s$, where z_s is the distance from focus, so that the resolution is given by a pure square-root law. For the architecture discussed here, instead, the infinite-NA trend which correctly reproduces the fidelity curves is

$$d(z_s) = \left(\frac{1}{z_s - z_a} - \frac{1}{z_s - z_b} \right)^{-1}, \tag{19}$$

as can be deduced from Eq. (17). In all cases, the performance of CPI outside of the planes in focus can be mathematically obtained by evaluating the infinite-NA fidelity $F_\infty(z_s, \sigma_s)$, and then inverting the implicit equation $F_\infty = c$.

Unlike the NA-independent image quality in the plane of sharpest refocusing, the axial sectioning enabled by refocusing is defined entirely by the NA, specifically by the same COC defining the imaging depth of conventional imaging systems. This results in a very interesting fact, namely, that the lateral and axial resolution are decoupled from each other, as summarized in the table below[4]:

	Lateral resolution		Axial resolution	
	In focus	Out of focus	In focus	Out of focus
STD imaging	$\frac{\lambda}{\mathrm{NA}}$	$|z - z_s|\,\mathrm{NA}$	$\frac{\text{lateral resolution}}{\mathrm{NA}}$	
CPI refocusing		$\sqrt{\lambda \, d(z_s)}$		

Although the resolution in the focused plane (or planes) of CPI is determined by the Rayleigh limit, as for standard (STD) imaging, the resolution limit when dealing with defocused objects is independent of the NA, as opposed to the COC-limited standard imaging. The dependence on NA, however, is critical when considering the axial component of the 3D resolution voxel, which has the same limitations as conventional imaging: both in focus (λ/NA^2) and out of focus (Eq. (15)) the axial resolution of CPI can be expressed as the ratio between the lateral resolution at a given z and the effective NA.

The decoupling of the spatial and lateral resolution enables the designs of optical setups characterized by high resolution, as defined by the CPI scheme of choice, with the sectioning capabilities that can be tuned independently by selecting the appropriate lens size. Such operation can even be performed in post-processing, by limiting the size of the refocusing integration path (Eq. (6)) to simulate a reduced *effective* NA, with no effect on resolution, for a deeper image reconstruction and improved computational efficiency. Such versatility sets CPI apart from conventional, lenslet-based, plenoptic imaging, which suffers from a strong trade-off between lateral and axial resolution [49, 65, 66].

Data Availibility Statement Not applicable

Declarations

Conflict of interest The author has no conflict of interest to declare that are relevant to the content of this article.

---

[4] The quantities reported in the table are obtained by neglecting proportionality constants.

References

1. V. Giovannetti, S. Lloyd, L. Maccone, Advances in quantum metrology. Nat. Photon. **5**, 222–229 (2011)
2. A. Zavatta, M. D'Angelo, V. Parigi, M. Bellini, Remote preparation of arbitrary time-encoded single-photon ebits. Phys. Rev. Lett. **96**, 020502 (2006)
3. T. Iskhakov, A. Allevi, D. Kalashnikov, V. Sala, M. Takeuchi, M. Bondani, M. Chekhova, Intensity correlations of thermal light: noise reduction measurements and new ghost imaging protocols. Euro. Phys. J. Spec. Top. **199**, 127–138 (2011)
4. A. Avella, I. Ruo-Berchera, I.P. Degiovanni, G. Brida, M. Genovese, Absolute calibration of an EMCCD camera by quantum correlation, linking photon counting to the analog regime. Opt. Lett. **41**, 1841–1844 (2016)
5. A. Agliati, M. Bondani, A. Andreoni, G. De Cillis, M.G.A. Paris, Quantum and classical correlations of intense beams of light investigated via joint photodetection. J. Opt. B: Quantum Semiclass. Opt. **7**(12), S652 (2005)
6. A. Allevi, S. Olivares, M. Bondani, Measuring high-order photon-number correlations in experiments with multimode pulsed quantum states. Phys. Rev. A **85**, 063835 (2012)
7. T.B. Pittman, Y.-H. Shih, D.V. Strekalov, A.V. Sergienko, Optical imaging by means of two-photon quantum entanglement. Phys. Rev. A **52**, 3429 (1995)
8. T. Pittman, D. Strekalov, D. Klyshko, M. Rubin, A. Sergienko, Y. Shih, Two-photon geometric optics. Phys. Rev. A **53**(4), 2804 (1996)
9. I.N. Agafonov, M.V. Chekhova, T.S. Iskhakov, L.-A. Wu, High-visibility intensity interference and ghost imaging with pseudo-thermal light. J. Mod. Opt. **56**, 422–431 (2009)
10. R.S. Aspden, D.S. Tasca, R.W. Boyd, M.J. Padgett, EPR-based ghost imaging using a single-photon-sensitive camera. New J. Phys. **15**, 073032 (2013)
11. M. Cassano, M. D'Angelo, A. Garuccio, T. Peng, Y. Shih, V. Tamma, Spatial interference between pairs of disjoint optical paths with a single chaotic source. Opt. Expr. **25**, 6589–6603 (2005)
12. Y. Bai, S. Han, Ghost imaging with thermal light by third-order correlation. Phys. Rev. A **76**(4), 043828 (2007)
13. M. Bina, D. Magatti, M. Molteni, A. Gatti, L.A. Lugiato, F. Ferri, Backscattering differential ghost imaging in turbid media. Phys. Rev. Lett. **110**, 083901 (2013)
14. G. Brida, M. Chekhova, G. Fornaro, M. Genovese, E. Lopaeva, I.R. Berchera, Systematic analysis of signal-to-noise ratio in bipartite ghost imaging with classical and quantum light. Phys. Rev. A **83**, 063807 (2011)
15. Y. Bromberg, O. Katz, Y. Silberberg, Ghost imaging with a single detector. Phys. Rev. A **79**(5), 053840 (2009)
16. K.W.C. Chan, M.N. O'Sullivan, R.W. Boyd, Two-color ghost imaging. Phys. Rev. A **79**, 033808 (2009)
17. M. D'Angelo, A. Valencia, M.H. Rubin, Y. Shih, Resolution of quantum and classical ghost imaging. Phys. Rev. A **72**(1), 013810 (2005)
18. B.I. Erkmen, J.H. Shapiro, Ghost imaging: from quantum to classical to computational. Adv. Opt. Photon. **2**(4), 405–450 (2010)
19. F. Ferri, D. Magatti, A. Gatti, M. Bache, E. Brambilla, L.A. Lugiato, High-resolution ghost image and ghost diffraction experiments with thermal light. Phys. Rev. Lett. **94**, 183602 (2005)
20. M. D'Angelo, A. Mazzilli, F.V. Pepe, A. Garuccio, V. Tamma, Characterization of two distant double-slits by chaotic light second order interference. Sci. Rep. **7**, 2247 (2017)
21. F. Ferri, D. Magatti, L. Lugiato, A. Gatti, Differential ghost imaging. Phys. Rev. Lett. **104**(25), 253603 (2010)
22. Y. Shih, The physics of turbulence-free ghost imaging. Technologies **4**(4), 39 (2016)
23. Z.-H. Xu, W. Chen, J. Penuelas, M. Padgett, M.-J. Sun, 1000 fps computational ghost imaging using LED-based structured illumination. Opt. Expr. **26**(3), 2427–2434 (2018)
24. A. Paniate, G. Massaro, A. Avella, A. Meda, F.V. Pepe, M. Genovese, M. D'Angelo, I. Ruo-Berchera, Light-field ghost imaging. Phys. Rev. Appl. **21**, 024032 (2024). https://doi.org/10.1103/PhysRevApplied.21.024032
25. P.-A. Moreau, E. Toninelli, T. Gregory, M.J. Padgett, Imaging with quantum states of light. Nat. Rev. Phys. **1**, 367–380 (2019)
26. G. Brida, M. Genovese, I. Ruo-Berchera, Experimental realization of sub-shot-noise quantum imaging. Nat. Photon. **4**, 227–230 (2010)
27. N. Samantaray, I. Ruo-Berchera, A. Meda, M. Genovese, Realization of the first sub-shot-noise wide field microscope. Light: Sci. & Appl. **6**(7), 17005 (2017)
28. G. Ortolano, A. Paniate, P. Boucher, C. Napoli, S. Soman, S.F. Pereira, I. Ruo-Berchera, M. Genovese, Quantum enhanced non-interferometric quantitative phase imaging. Light: Sci. & Appl. **12**(1), 171 (2023). https://doi.org/10.1038/s41377-023-01215-1
29. A. Allevi, S. Cassina, M. Bondani, Super-thermal light for imaging applications. Quantum Measur. Quantum Metrol. **4**(1), 26–34 (2017)
30. A. Gatti, E. Brambilla, M. Bache, L.A. Lugiato, Ghost imaging with thermal light: comparing entanglement and classical correlation. Phys. Rev. Lett. **93**, 093602 (2004)
31. M.N. O'Sullivan, K.W.C. Chan, R.W. Boyd, Comparison of the signal-to-noise characteristics of quantum versus thermal ghost imaging. Phys. Rev. A **82**, 053803 (2010)
32. A. Valencia, G. Scarcelli, M. D'Angelo, Y. Shih, Two-photon imaging with thermal light. Phys. Rev. Lett. **94**, 063601 (2005)
33. M. D'Angelo, F.V. Pepe, A. Garuccio, G. Scarcelli, Correlation plenoptic imaging. Phys. Rev. Lett. **116**, 223602 (2016)
34. G. Massaro, D. Giannella, A. Scagliola, F. Di Lena, G. Scarcelli, A. Garuccio, F.V. Pepe, M. D'Angelo, Light-field microscopy with correlated beams for high-resolution volumetric imaging. Sci. Rep. **12**, 16823 (2022)
35. G. Massaro, P. Mos, S. Vasiukov, F.D. Lena, F. Scattarella, F.V. Pepe, A. Ulku, D. Giannella, E. Charbon, C. Bruschini, M. D'Angelo, Correlated-photon imaging at 10 volumetric images per second. Sci. Rep. **13**, 12813 (2023)
36. C. Abbattista, L. Amoruso, S. Burri, E. Charbon, F. Di Lena, A. Garuccio, D. Giannella, Z. Hradil, M. Iacobellis, G. Massaro et al., Towards quantum 3D imaging devices. Appl. Sci. **11**(14), 6414 (2021). https://doi.org/10.3390/app11146414
37. F. Scattarella, D. Diacono, A. Monaco, N. Amoroso, L. Bellantuono, G. Massaro, F.V. Pepe, S. Tangaro, R. Bellotti, M. D'Angelo, Deep learning approach for denoising low-SNR correlation plenoptic images. Sci. Rep. **13**(1), 19645 (2023). https://doi.org/10.1038/s41598-023-46765-x
38. I. Petrelli, F. Santoro, G. Massaro, F. Scattarella, F.V. Pepe, F. Mazzia, M. Ieronymaki, G. Filios, D. Mylonas, N. Pappas, C. Abbattista, M. D'Angelo, Compressive sensing-based correlation plenoptic imaging. Front. Phys. **11**, 1287740 (2023). https://doi.org/10.3389/fphy.2023.1287740

39. F.V. Pepe, F. Di Lena, A. Mazzilli, E. Edrei, A. Garuccio, G. Scarcelli, M. D'Angelo, Diffraction-limited plenoptic imaging with correlated light. Phys. Rev. Lett. **119**, 243602 (2017)
40. E.H. Adelson, J.Y.A. Wang, Single lens stereo with a plenoptic camera. IEEE Trans. Pattern Anal. Mach. Intell. **14**, 99–106 (1992). https://doi.org/10.1109/34.121783
41. J. Pawley, *Handbook of biological confocal microscopy* (Springer, Berlin, 2006). https://doi.org/10.1007/978-1-4757-5348-6
42. I. Ihrke, J. Restrepo, L. Mignard-Debise, Principles of light field imaging: briefly revisiting 25 years of research. IEEE Signal Process. Mag. **33**(5), 59–69 (2016)
43. R. Ng, M. Levoy, M. Brédif, G. Duval, M. Horowitz, P. Hanrahan, Light field photography with a hand-held plenoptic camera. Computer Science Technical Report CSTR **2**, 1–11 (2005)
44. R. Ng, Fourier slice photography. ACM Transactions on Graphics **24**(3), 735–744 (2005). ACM
45. C. Birklbauer, O. Bimber, Panorama light-field imaging. Comput. Gr. Forum **33**, 43–52 (2014). https://doi.org/10.1111/cgf.12289
46. M. Broxton, L. Grosenick, S. Yang, N. Cohen, A. Andalman, K. Deisseroth, M. Levoy, Wave optics theory and 3-D deconvolution for the light field microscope. Opt. Expr. **21**, 25418–25439 (2013)
47. R. Prevedel, Y.-G. Yoon, M. Hoffmann, N. Pak, G. Wetzstein, S. Kato, T. Schrödel, R. Raskar, M. Zimmer, E.S. Boyden et al., Simultaneous whole-animal 3D imaging of neuronal activity using light-field microscopy. Nat. Methods **11**(7), 727–730 (2014)
48. T. Georgeiv, K.C. Zheng, B. Curless, D. Salesin, S. Nayar, C. Intwala, Spatio-angular resolution tradeoffs in integral photography. In: Proceedings of the 17th eurographics conference on rendering techniques. EGSR '06, pp. 263–272. Eurographics Association, Goslar, DEU (2006)
49. B. Goldlücke, O. Klehm, S. Wanner, E. Eisemann, Plenoptic cameras, in *Digital representations of the real world: how to capture, model, and render visual reality*. ed. by M. Magnor, O. Grau, O. Sorkine-Hornung, C. Theobalt (CRC Press, Boca Racton, 2015)
50. G. Massaro, F.V. Pepe, M. D'Angelo, Refocusing algorithm for correlation plenoptic imaging. Sensors **22**, 6665 (2022)
51. G. Massaro, B. Barile, G. Scarcelli, F.V. Pepe, G.P. Nicchia, M. D'Angelo, Direct 3D imaging through spatial coherence of light. Laser Photon. Rev. **18**, 2301155 (2024). https://doi.org/10.1002/lpor.202301155
52. G. Massaro, F. Di Lena, M. D'Angelo, F.V. Pepe, Effect of finite-sized optical components and pixels on light-field imaging through correlated light. Sensors **22**(7), 2778 (2022). https://doi.org/10.3390/s22072778
53. F.V. Pepe, F. Di Lena, A. Garuccio, G. Scarcelli, M. D'Angelo, Correlation plenoptic imaging with entangled photons. Technologies **4**, 17 (2016)
54. F. Di Lena, F. Pepe, A. Garuccio, M. D'Angelo, Correlation plenoptic imaging: an overview. Appl. Sci. **8**(10), 1958 (2018). https://doi.org/10.3390/app8101958
55. F. Di Lena, G. Massaro, A. Lupo, A. Garuccio, F.V. Pepe, M. D'Angelo, Correlation plenoptic imaging between arbitrary planes. Opt. Expr. **28**, 35857–35868 (2020)
56. D. Giannella, G. Massaro, B. Stoklasa, M. D'Angelo, F.V. Pepe, Light-field imaging from position-momentum correlations. Phys. Lett. A **494**, 129298 (2024). https://doi.org/10.1016/j.physleta.2023.129298
57. G. Massaro, G. Scala, M. D'Angelo, F.V. Pepe, Comparative analysis of signal-to-noise ratio in correlation plenoptic imaging architectures. Euro. Phys. J. Plus **137**, 1123 (2022)
58. G. Scala, M. D'Angelo, A. Garuccio, S. Pascazio, F.V. Pepe, Signal-to-noise properties of correlation plenoptic imaging with chaotic light. Phys. Rev. A **99**, 053808 (2019)
59. R. Clackdoyle, M. Defrise, Tomographic reconstruction in the 21st century. IEEE Signal Process. Mag. **27**(4), 60–80 (2010). https://doi.org/10.1109/MSP.2010.936743
60. M. Levoy, Volume Rendering Using the Fourier projection-slice theorem. Computer systems laboratory, Stanford University (1992)
61. P.A. Stokseth, Properties of a defocused optical system. J. Opt. Soc. Am. **59**(10), 1314–1321 (1969). https://doi.org/10.1364/JOSA.59.001314
62. D.B. Murphy, M.W. Davidson, *Diffraction and spatial resolution* (John Wiley & Sons Ltd, NJ, 2012), pp.103–113
63. F. Scattarella, M. D'Angelo, F.V. Pepe, Resolution limit of correlation plenoptic imaging between arbitrary planes. Optics **3**, 138–149 (2022)
64. F. Scattarella, G. Massaro, B. Stoklasa, M. D'Angelo, F.V. Pepe, Periodic patterns for resolution limit characterization of correlation plenoptic imaging. Euro. Phys. J. Plus **138**(8), 710 (2023). https://doi.org/10.1140/epjp/s13360-023-04322-5
65. D.G. Dansereau, O. Pizarro, S.B. Williams, Decoding, calibration and rectification for lenselet-based plenoptic cameras. In: Proceedings of the IEEE conference on computer vision and pattern recognition, pp. 1027–1034 (2013)
66. T.G. Georgiev, A. Lumsdaine, S. Goma, High Dynamic Range Image Capture with Plenoptic 2.0 Camera. In: Frontiers in optics 2009/laser science XXV/fall 2009 OSA optics & photonics technical digest, p. 7. Optical Society of America, Washington, DC (2009)